Bioactive Materials 41 (2024) 597–610

Contents lists available at ScienceDirect

Bioactive Materials

journal homepage: www.keaipublishing.com/en/journals/bioactive-materials

ROS-sensitive PD-L1 siRNA cationic selenide nanogels for self-inhibition of autophagy and prevention of immune escape

Jie Gao [b,c,1,***], Yonghua Zhai [d,1], Weihong Lu [a,**,1], Xianghe Jiang [d,1], Jingsheng Zhou [b,c,d], Lili Wu [b,c], Longhai Du [e], Chunqing Ou [b,c], Xinyi Zhang [b,c], Hanliang He [f], Jian Zhu [a], Zhengbiao Zhang [a], Meiyun Li [d], Yan Wu [d,****], Xiangqiang Pan [a,d,*]

[a] State and Local Joint Engineering Laboratory for Novel Functional Polymeric Materials, Jiangsu Key Laboratory of Advanced Functional Polymer Design and Application, College of Chemistry, Chemical Engineering and Materials Science, Soochow University, Suzhou, 215123, China
[b] Changhai Clinical Research Unit, Shanghai Changhai Hospital, Naval Medical University, Shanghai, 200433, China
[c] Shanghai Key Laboratory of Nautical Medicine and Translation of Drugs and Medical Devices, Shanghai, 200433, China
[d] College of Life Science, Mudanjiang Medical University, Mudanjiang, 157011, China
[e] Department of Orthopedics, Jinshan Hospital, Fudan University, Shanghai, 201508, China
[f] The Department of Orthopedic Surgery, Dushu Lake Hospital Affiliated to Soochow University, Suzhou, 215028, China

ARTICLE INFO

Keywords:
Multicomponent reaction
ROS sensitive
Cationic nanogel
Autophagy inhibition
Immune escape

ABSTRACT

In the field of cancer therapy, inhibiting autophagy has emerged as a promising strategy. However, pharmacological disruption of autophagy can lead to the upregulation of programmed death-ligand 1 (PD-L1), enabling tumor immune evasion. To address this issue, we developed innovative ROS-responsive cationic poly(ethylene imine) (PEI) nanogels using selenol chemistry-mediated multicomponent reaction (MCR) technology. This procedure involved simple mixing of low-molecular-weight PEI (LMW PEI), γ-selenobutylacetone (γ-SBL), and poly (ethylene glycol) methacrylate (PEGMA). Through high-throughput screening, we constructed a library of $A_xSe_yO_z$ nanogels and identified the optimized $A_{1.8}Se_3O_{0.5}$/siPD-L1 nanogels, which exhibited a size of approximately 200 nm, excellent colloidal stability, and the most effective PD-L1 silencing efficacy. These nanogels demonstrated enhanced uptake by tumor cells, excellent oxidative degradation ability, and inhibited autophagy by alkalinizing lysosomes. The $A_{1.8}Se_3O_{0.5}$/siPD-L1 nanogels significantly downregulated PD-L1 expression and increased the expression of major histocompatibility complex class I (MHC-I), resulting in robust proliferation of specific $CD8^+$ T cells and a decrease in MC38 tumor growth. As a result, the $A_{1.8}Se_3O_{0.5}$/siPD-L1 nanogels inhibited tumor growth through self-inhibition of autophagy, upregulation of MHC-I, and downregulation of PD-L1. Designed with dynamic diselenide bonds, the $A_{1.8}Se_3O_{0.5}$/siPD-L1 nanogels showed synergistic antitumor efficacy through self-inhibition of autophagy and prevention of immune escape.

1. Introduction

Autophagy plays a critical role in development and metastasis by removing damaged cells and degrading immune-activating molecules, such as major histocompatibility complex class I (MHC-I) [1,2]. In cancer therapy, strategies based on autophagy inhibition have been widely used to prevent tumor progression and metastasis [3–7]. Despite demonstrating promising antitumor efficacy in vitro, the effectiveness of autophagy inhibition in vivo remains unsatisfactory [8–11]. One significant reason for this difference is that inhibiting autophagy leads to an increase in the expression of PD-L1 on the surface of tumor cells. This upregulated PD-L1 exacerbates immunosuppression and immune

Peer review under responsibility of KeAi Communications Co., Ltd.
* Corresponding author. College of Chemistry, Chemical Engineering and Materials Science, Soochow University, Suzhou, 215123, China.
** Corresponding author.
*** Corresponding author. Changhai Clinical Research Unit, Shanghai Changhai Hospital, Naval Medical University, Shanghai, 200433, China.
**** Corresponding author. College of Life Science, Mudanjiang Medical University, Mudanjiang, 157011, China.
E-mail addresses: gaojiehighclea@smmu.edu.cn (J. Gao), luweihong@suda.edu.cn (W. Lu), wuyan@mdjmu.edu.cn (Y. Wu), panxq@suda.edu.cn (X. Pan).
[1] These authors contributed equally to this paper.

https://doi.org/10.1016/j.bioactmat.2024.08.013
Received 22 February 2024; Received in revised form 14 August 2024; Accepted 15 August 2024

tolerance within cancer cells, leading to significant immune evasion [12]. Therefore, developing a feasible strategy capable of simultaneously inhibiting both autophagy and upregulating PD-L1 is crucial [13–15].

Polyethylenimine (PEI) has significant pH-responsive "proton sponge" effects, leading to alkalization and impairment of lysosomal function, suggesting that it is an effective autophagy inhibitor [16,17]. Additionally, PEI is widely utilized as a transfection agent for gene delivery [15,18,19]. Therefore, condensing PEI with siRNA targeting PD-L1 (siPD-L1) has the potential to downregulate PD-L1 by blocking the PD-1/PD-L1 immune checkpoint and synergistically inhibiting autophagy, thereby enhancing antitumor therapy via autophagy inhibition. Low-molecular-weight PEI has reduced transfection efficiency due to its relatively low molecular weight [20]. However, this drawback is offset by its enhanced metabolic clearance and elimination within the body, which results in comparatively superior biocompatibility and reduced cellular toxicity [21]. On the other hand, high-molecular-weight PEI, due to its larger molecular weight, facilitates more efficient formation of nucleic acid complexes and enables effective gene delivery within cells, leading to heightened transfection efficiency [15]. It is important to note that the greater molecular weight and polycationic properties of high-molecular-weight PEI may induce greater cellular membrane disruption, consequently increasing cellular toxicity [17,22,23]. To address this limitation, intelligent degradable cationic polymers with sufficient charge density and the ability to decompose into small fragments in a physiological environment are desirable. These polymers are expected to exhibit high gene transfection efficiency and low cytotoxicity [24]. In the tumor microenvironment (TME), there is an excess of reactive oxygen species (ROS), such as H_2O_2, superoxide anions (O_2^-), and hydroxyl radicals [25–28]. Leveraging this characteristic, several ROS stimulus-responsive polymers based on PEI modification have been designed to specifically target tumors for gene transfection [29–31]. However, the complex synthesis steps of functional PEI present technical and manufacturing challenges, making it desirable to streamline the synthesis process.

In this study, we present the development of a new diselenide-crosslinked PEI nanogel using a simple selenol-based combinatorial synthesis method [32]. This nanogel effectively condenses siPD-L1 to enhance antitumor efficacy by inhibiting autophagy while simultaneously knocking down PD-L1 to overcome autophagy-induced immune escape. We created a library of ROS-sensitive cationic nanogels ($A_xSe_yO_z$) using a rapid one-pot two-step multicomponent reaction (MCR) with selenol generated by γ-selenobutyrolactone (SBL) in situ. Due to the presence of dynamic diselenide bonds, nanogels could be formed upon ultrasound stimulation for subsequent RNA encapsulation. To determine the efficiency of siRNA transfection in the tumor microenvironment, siPD-L1 was condensed into nanogels through electrostatic adsorption of the numerous amine groups of PEI under physiological conditions (pH~7.4) (Scheme 1A). Upon entering the tumor microenvironment, the optimized $A_{1.8}Se_3O_{0.5}$/siPD-L1 nanogels

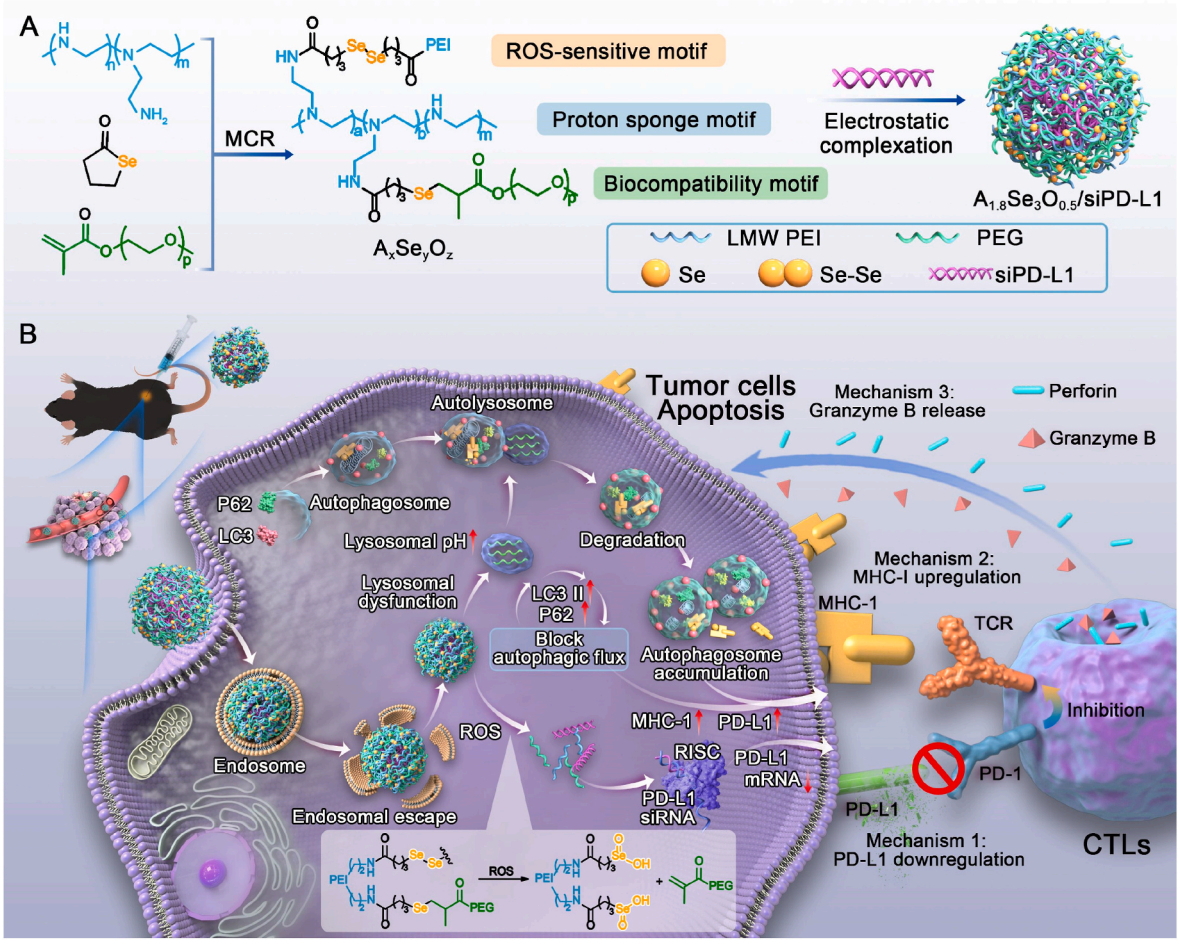

Scheme 1. Schematic illustration of the preparation and antitumor mechanisms of the $A_{1.8}Se_3O_{0.5}$/siPD-L1 nanogels. Nanogels with three features (ROS sensitivity, proton sponge ability, and biocompatibility) were synthesized using selenol chemistry-mediated multicomponent reaction (MCR) technology with LMW PEI, γ-SBL, and PEGMA. After electrostatic complexation with siRNA, $A_{1.8}Se_3O_{0.5}$/siPD-L1 nanogels were formed. These nanogels demonstrated improved uptake by tumor cells and underwent endosomal escape and siRNA release in an intracellular oxidative environment, resulting in the downregulation of PD-L1 and increased expression of major histocompatibility complex class I (MHC-I). Ultimately, $CD8^+$ T cells are activated and induce tumor cell death by secreting granzyme B.

exhibit endosomal escape and release siRNA due to nanogel degradation *via* ROS stimulation and the proton sponge effects of PEI. PEI self-inhibited autophagy and degraded MHC-I through alkalinized lysosomes, while siRD-L1 efficiently knocked down PD-L1 to prevent immune escape (Scheme 1B). The $A_{1.8}Se_3O_{0.5}$/siPD-L1 nanogels significantly inhibited tumor growth, enhancing autophagy inhibition and PD-L1 downregulation-based therapeutic efficacy through self-inhibition of autophagy, upregulation of MHC-I, and downregulation of PD-L1 to prevent immune escape. Therefore, PD-L1 siRNA-loaded PEI nanogels, which are designed with dynamic diselenide bonds, could show synergistic antitumor efficacy through self-inhibition of autophagy and prevention of immune escape. Tumor-derived PD-L1 plays a key role in immunosuppression, and PD-L1 on MC38 colorectal adenocarcinoma cells is sufficient to suppress antitumor immunity compared to that on tumor cells such as B16 melanoma cells [33]. In immunogenic MC38 tumors, PD-L1 plays a dominant role in suppressing tumor immunity, and PD-L1 on tumor cells suppresses tumor immunity mainly by inhibiting the cytotoxicity of $CD8^+$ T cells [34]. Therefore, we selected MC38 cells to evaluate the efficacy of siPD-L1. Given the significant role of PD-L1 in modulating immune reactions, we chose MC38 cells as a model to assess the therapeutic potential of siPD-L1, a strategy aimed at silencing PD-L1 expression and thereby enhancing the immune system's capacity to combat cancer [33–36].

2. Results and discussion

2.1. Preparation and characterization of $A_xSe_yO_z$ nanogels through a multicomponent reaction (MCR)

To create an efficient siRNA delivery platform, we developed a selenol chemistry-mediated multicomponent reaction (MCR) for the simultaneous coupling of LMW-PEI, poly(ethylene glycol) methacrylate (PEGMA), and γ-selenobutyrolactone (SBL) (Scheme 1, Fig. 1A). With its excess amino groups, LMW-PEI was found to be alkaline in aqueous solution (2 wt% PEI-1800, pH > 12), significantly enhancing the nucleophilic aminolysis reaction of SBL, as well as the subsequent selenol oxidation coupling reaction and nucleophilic selenol-ene reaction. This process facilitated the exclusive ring-opening reaction of SBL with PEI in aqueous media. Notably, the reaction proceeded rapidly without the need for any additives or specific reaction conditions, with complete conversion of SBL achieved in just 10 min of shaking at room temperature (Table S1, Figs. S1 and S3).

PEGMA was used as a representative functional acrylate component in MCR for high-throughput screening of siRNA vectors owing to its reduced toxicity and prolonged blood circulation time during transfection [37]. A molar ratio of 1:3:1 was used for the three building blocks PEI1800, SBL, and PEGMA500, and the reaction process was monitored via ^{1}H NMR spectroscopy (Fig. S1). The methylene proton signals on SBL shifted completely from 3.52, 2.46, and 2.25 ppm to 3.33, 2.30, and 1.92 ppm, respectively, while the acrylate proton signals of PEGMA500 vanished completely with adjacent methyl signals shifting from 1.96 ppm to 1.28 ppm, indicating the complete conversion of SBL to PEGMA500. Additionally, the remaining selenols spontaneously couple in air to form diselenide dynamic covalent bonds, allowing LMW PEI to cross-link to the hydrogel. The $A_{1.8}Se_3O_{0.5}$ cationic polymer structure was also further verified by FT-IR spectroscopy (Fig. S2). This MCR approach represents an innovative and versatile synthesis toolkit that enables easy and rapid synthesis of a diverse library of nanogels, thereby avoiding intricate experimental procedures, additional unfriendly reagents, and laborious postprocessing steps (Fig. S3). Furthermore, various functional groups, such as fluorophores, can be easily introduced (Fig. S4). Accordingly, this strategy facilitated the design of a combinatorial chemistry experiment in which three molecular weights of PEI, three molecular weights of PEGMA, and four different proportions of SBL were used to directly synthesize 36 kinds of hydrogels in a 48-well plate in 10 min.

The stability and biocompatibility of nanogels in biological fluids have been demonstrated by numerous studies, highlighting their

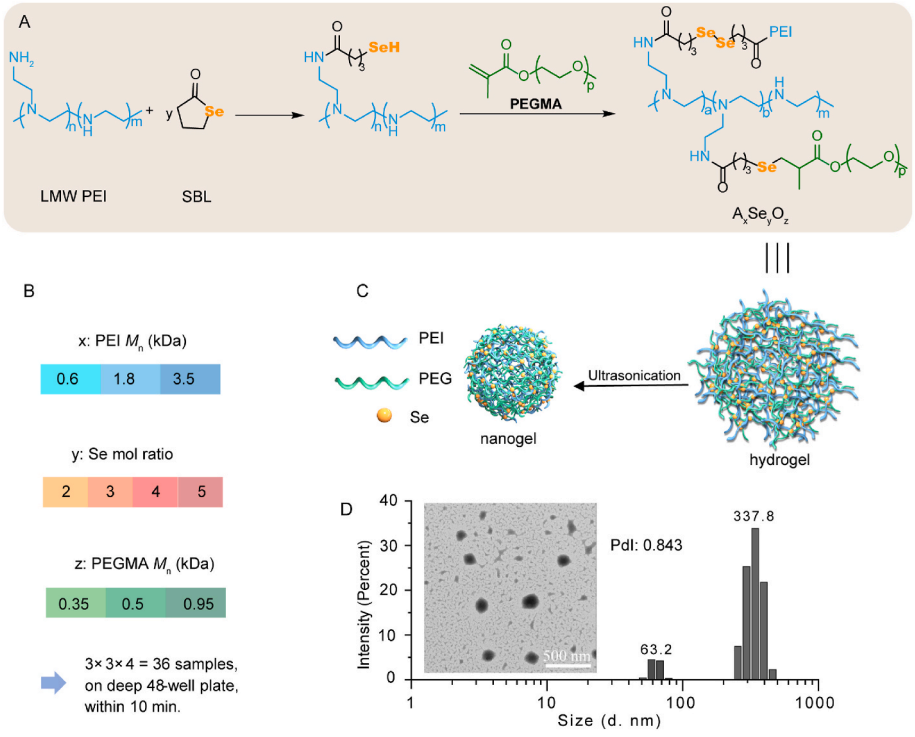

Fig. 1. Schematic illustration of selenol chemistry-mediated MCR for high-throughput synthesis of nanogels. (A) Proposed reaction process of selenol chemistry-mediated MCR. (B) Structures of the three components of LMW PEI, PEGMA and SBL used for the synthesis library of nanogels, which were defined as $A_xSe_yO_z$ (x denotes the MW (kDa) of the PEI, y denotes the molar ratio of SBL/PEI, and z denotes the MW (kDa) of the PEGMA). (C) The dispersion-ultrasonic dilution approach for nanogel preparation. (D) Representative TEM image and DLS size distribution of the $A_{1.8}Se_3O_{0.5}$ nanogels; scale bars = 500 nm.

flexibility and pliability, which render them more permeable than rigid nanoparticles [38–43]. However, the preparation of nanogels is also relatively intricate, and the postfunctionalization modification process is cumbersome, thereby impeding large-scale screening [44–46]. With our technology, nanogels can be readily prepared through the dynamic exchange of diselenide covalent bonds by dispersing the hydrogel in water and ultrasonication (Fig. 1C). Dynamic light scattering (DLS) showed that only nanoparticles were present in the dispersion system without significant aggregation (Fig. 1D). This result was also confirmed by transmission electron microscopy (TEM), which did not affect the subsequent letrostastic complexation with siRNA, although the nanoparticles were not uniformly distributed (Fig. 2G). Thus, we present the first instance of nanogel preparation through a dynamic covalent bond exchange reaction. The straightforward and highly efficient preparation process renders this method particularly suitable for the comprehensive assessment of carrier properties on a large scale.

The nanogel naturally exhibited a highly sensitive redox response in the presence of (di)selenide, and its responsiveness was confirmed by a variety of characterizations. In the ^{1}H NMR spectra, proton signals at 6.4 ppm and 5.8 ppm originating from the PEGMA building block were clearly evident upon treatment with hydrogen peroxide (100 μM). After the oxidation process using hydrogen peroxide for GPC analysis, the results indicated that the polymer's molecular weight was 3300 g mol^{-1}, slightly higher than that of PEI before the reaction. (Fig. S5). The results suggest that the oxidative degradation of the nanogels can be initiated by a low concentration of hydrogen peroxide close to the environment of

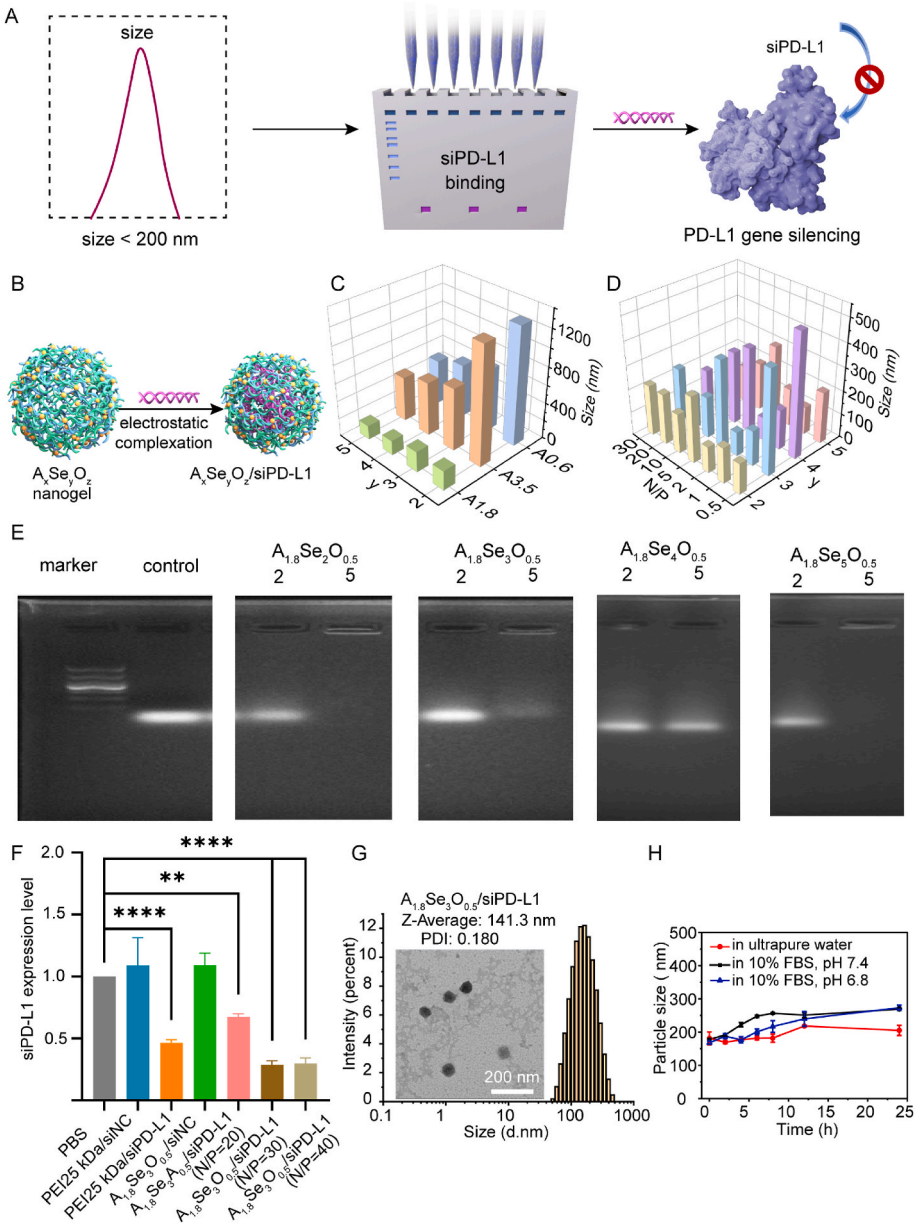

Fig. 2. Throughput screening of the $A_xSe_yO_z$ nanogel for in vitro siPD-L1 delivery and characterization of the optimized $A_{1.8}Se_3O_{0.5}$/siPD-L1 nanogels. (A) Schematic illustrating the workflow for screening and (B) preparation of the nanogels. (C) Dynamic light scattering measurements (n = 3) for $A_xSe_yO_{0.5}$/siPD-L1 nanogels (PEI_{1800}, PEI_{3500} or PEI_{600}; $PEGMA_{500}$; y = 2–5) and (D) $A_{1.8}Se_yO_{0.5}$/siPD-L1 nanogels (PEI_{1800}, $PEGMA_{500}$; y = 2–5; N/P = 0.5–30). (E) Excerpted gel electrophoresis assay for $A_{1.8}Se_yO_{0.5}$/siPD-L1, y = 2–5, N/P = 2 or 5. The results of the full gel electrophoresis assay are shown in Fig. S10. (F) Gene silencing of optimized $A_{1.8}Se_3O_{0.5}$/siPD-L1, N/P = 20–40. (G) TEM image and DLS image of the top siPD-L1-expressing nanogel ($A_{1.8}Se_3O_{0.5}$/siPD-L1, N/P = 30); scale bar = 200 nm. (H) Stability of the $A_{1.8}Se_3O_{0.5}$/siPD-L1 nanogel in 10 % FBS-PBS at pH 7.4 and pH 6.8 and ultrapure water demonstrated by DLS within 24 h, N/P = 30. The data are presented as the means ± SDs (n = 3).

tumor cells, leading to subsequent release of PEGMA and retaining attachment of selenium fragments to the PEI main chain [47]. The ^{77}Se NMR spectra revealed that the original coexisting selenide and diselenide exhibited peak positions at 136 and 292 ppm, respectively (Fig. S6). Upon oxidation, the products undergo complete degradation to yield selenite acid with a signal at 1181 ppm. Furthermore, diselenide can be reduced to selenol by treatment with dithiothreitol, resulting in a shift of the selenium signal peak to −165 ppm. The TEM results also showed that there was no obvious aggregation (Fig. S7). All this evidence indicated that the nanogels were degraded under either oxidative or reducing conditions (Fig. S8), which is beneficial for promoting cellular uptake and reducing the toxicity of PEI nanogels [48].

2.2. Transfection efficiency through screening of $A_xSe_yO_z$ nanogels

The degradation of siRNA by serum nucleases can be reduced by using cationic delivery vehicles [49]. PEI has been suggested to prevent endosomal degradation by acting as a "proton sponge" and can bind with negatively charged siRNA through electrostatic interactions, forming stable nanoscale colloidal complexes [20]. In this study, we used $A_xSe_yO_z$ as a vehicle for optimizing siRNA delivery vectors via a combinatorial chemistry throughput screening strategy, considering the good biocompatibility of PEG. The screening process involved evaluating the particle size, gel retardation, and gene silencing efficiency (Fig. 2A), and the optimization was performed based on the nanoparticle size, transfection efficiency, toxicity, and stability to determine the best formulation.

The influence of the PEI molecular weight and crosslinking density on the efficiency of the siRNA complex was first examined. When the molecular weight of PEI was 1800 g mol^{-1}, the particle size of the nanogel remained consistent within 200 nm regardless of the Se molar ratio (2–5) or N/P ratio (10–30) (Fig. 2B and **C**). On the other hand, when the molecular weight of PEI was 600 or 3500 g mol^{-1}, the particle size was significantly larger or did not meet the DLS test requirements directly (Tables S2, S3, S4 and S5). This indicated that the PEI molecular weight significantly affected siRNA electrostatic complexation, likely due to the length of the hydrophilic chains and the charge distribution within the cationic nanogels. Additionally, siRNA nanogels with a suitable particle size (approximately 200 nm or smaller) were more likely to be obtained with a PEG molecular weight of 500 g mol^{-1} than with 300 or 950 g mol^{-1} (Figs. 2D and S9, Table S5). The retardation assays showed excellent condensation by the vehicles when the N/P ratio exceeded 10 after incubation with siRNA at varying N/P ratios (Figs. 2E and S10). At an N/P ratio of 20, complete condensation of the siRNA was achieved by $A_{1.8}Se_yO_{0.5}$ (y = 2–5), as confirmed by a gel retardation assay. Notably, as shown in Fig. 2F, compared with that of commercial Jet PEI, the vehicle architecture of $A_{1.8}Se_3O_{0.5}$ had a 29 % greater gene silencing efficiency (48 %) (Fig. S11).

The optimized $A_{1.8}Se_3O_{0.5}$/siPD-L1 nanogel had a hydrated particle size of 141 nm, with a narrow particle size distribution and a zeta potential of 30.8 mV (Figs. 2G and S12). TEM analysis revealed a reduced particle size of approximately 70 nm. Electrostatic complexation with siPD-L1 promoted a homogeneous distribution of nanoparticles compared with that of the naked nanogel. Furthermore, this nanogel demonstrated excellent colloidal stability for 24 h in both 10 % FBS and ultrapure water (Fig. 2H). Even after storage in ultrapure water for 21 days, the optimized nanogel maintained its superior colloidal stability, highlighting the robust interaction between the vehicle and siRNA (Fig. S13). Additionally, the results demonstrated that the nanogels exhibited moderate expansion in 10 % fetal bovine serum at pH 7.4 and 6.8 within a 24-h period. This observation suggested that nanogels can be stably transported within the body and maintain structural and functional integrity in the tumor microenvironment. When simulating the intracellular reactive oxygen species (ROS) concentration in tumor cells (100 μM H_2O_2), we observed that siRNA release approached 80 % within 4 h, whereas in the absence of oxidants, the release did not exceed 25 %. These findings are consistent with those reported in the literature [48,50]. (Fig. S14). TEM images of $A_{1.8}Se_3O_{0.5}$/siPD-L1 nanogels treated with H_2O_2 were used to visualize the dissociation of the complexes (Fig. S15). These results suggest that the nanocomplexes exhibit a sensitive oxidative response.

2.3. $A_{1.8}Se_3O_{0.5}$/siPD-L1 inhibits autophagy through alkaline lysosomes and ultimately upregulates MHC-1 expression

In our initial investigation, we examined the uptake efficiency of $A_{1.8}Se_3O_{0.5}$/siRNA nanogels in MC38 colon tumor cells using Cy3-labeled siRNA to track cellular uptake. The $A_{1.8}Se_3O_{0.5}$/Cy3 siRNA group demonstrated significantly greater cellular uptake efficiency than did the PEI 25 kDa/Cy3 siRNA group, as depicted in Fig. 3A and **B** ($P < 0.05$). As the positively charged amino groups of PEI can potentially increase lysosomal pH [51], we further explored the effect of the $A_{1.8}Se_3O_{0.5}$/siRNA nanogels on lysosomal pH by staining with LysoSensor Green DND-189, a fluorescent pH indicator. As shown in Fig. 3C and **D**, compared with control cells, $A_{1.8}Se_3O_{0.5}$/siNC or $A_{1.8}Se_3O_{0.5}$/siPD-L1 significantly increased the lysosomal pH, as indicated by the markedly decreased fluorescence intensity. Additionally, damage to lysosomes by chloroquine (CQ), a lysosomal inhibitor, was evident through an increase in lysosomal pH. Subsequently, we utilized the adeno-associated virus mRFP-GFP-LC3 to monitor autophagic flux (Fig. 3E). As shown in Fig. 3F, exposure to $A_{1.8}Se_3O_{0.5}$/siNC or $A_{1.8}Se_3O_{0.5}$/siPD-L1 substantially increased the number of autophagosomes (APs) and decreased the accumulation of autolysosomes (ALs), suggesting dysfunctional autophagic flux in cells incubated with the nanogels. Furthermore, we investigated the impact of $A_{1.8}Se_3O_{0.5}$/siRNA nanogels on autophagy-related proteins, including LC3 and P62/SQSTM1. The total amount of LC3 protein or the LC3-II/LC3-I ratio can reflect the level of autophagy. P62/SQSTM1 (P62), a versatile adaptor protein, is a selective autophagy receptor [52–54]. Western blotting analysis (Fig. 3G and **H**) revealed elevated expression levels of lipid-bound LC3-II and the autophagy substrate SQSTM1/p62 in cells treated with $A_{1.8}Se_3O_{0.5}$/siNC or $A_{1.8}Se_3O_{0.5}$/siPD-L1, indicating the inhibition of autophagic flux. The accumulation of LC3-II and SQSTM1/p62 after nanogel treatment was also confirmed by fluorescence microscopy (Fig. S17). In addition, we observed the LC3-I/LC3-II ratio in cells treated with both CQ and $A_{1.8}Se_3O_{0.5}$ to determine the changes in cellular autophagy under different interventions. Using Western blot analysis of cell lysates, we observed that the combined application of CQ and $A_{1.8}Se_3O_{0.5}$, as well as the application of $A_{1.8}Se_3O_{0.5}$/siPD-L1, did not significantly influence the conversion of LC3-I to LC3-II. These findings suggest that the concurrent administration of two drugs with overlapping mechanisms may not confer an additive therapeutic benefit (Fig. S18). In conclusion, our findings demonstrate that $A_{1.8}Se_3O_{0.5}$/siRNA nanogels efficiently enter tumor cells, induce lysosome alkalinization, and inhibit autophagic flux, suggesting their potential for modulating cellular processes and potentially serving as therapeutic tools in cancer treatment.

Previous studies have demonstrated that MHC-I molecules in tumor cells are targeted for lysosomal degradation through an autophagy-dependent mechanism, resulting in decreased expression of MHC-I on the cell surface and predominant localization within autophagosomes and lysosomes [1]. Importantly, inhibiting autophagy has been shown to restore the levels of MHC-I on the cell surface and enhance antigen presentation [55]. Based on these findings, we hypothesized that the autophagy inhibitory effects of the $A_{1.8}Se_3O_{0.5}$ nanogels could lead to the restoration of MHC-I expression in MC38 cells. As depicted in Fig. 3I and **J**, the flow cytometry results demonstrated that RAP decreased the expression of MHC-I, while the nanogels and CQ significantly upregulated the expression of MHC-I molecules.

Our findings indicate that $A_{1.8}Se_3O_{0.5}$/siRNA nanogels efficiently enter tumor cells, inducing lysosome alkalinization, inhibiting autophagy, and upregulating MHC-I expression. Additionally, the nanogels

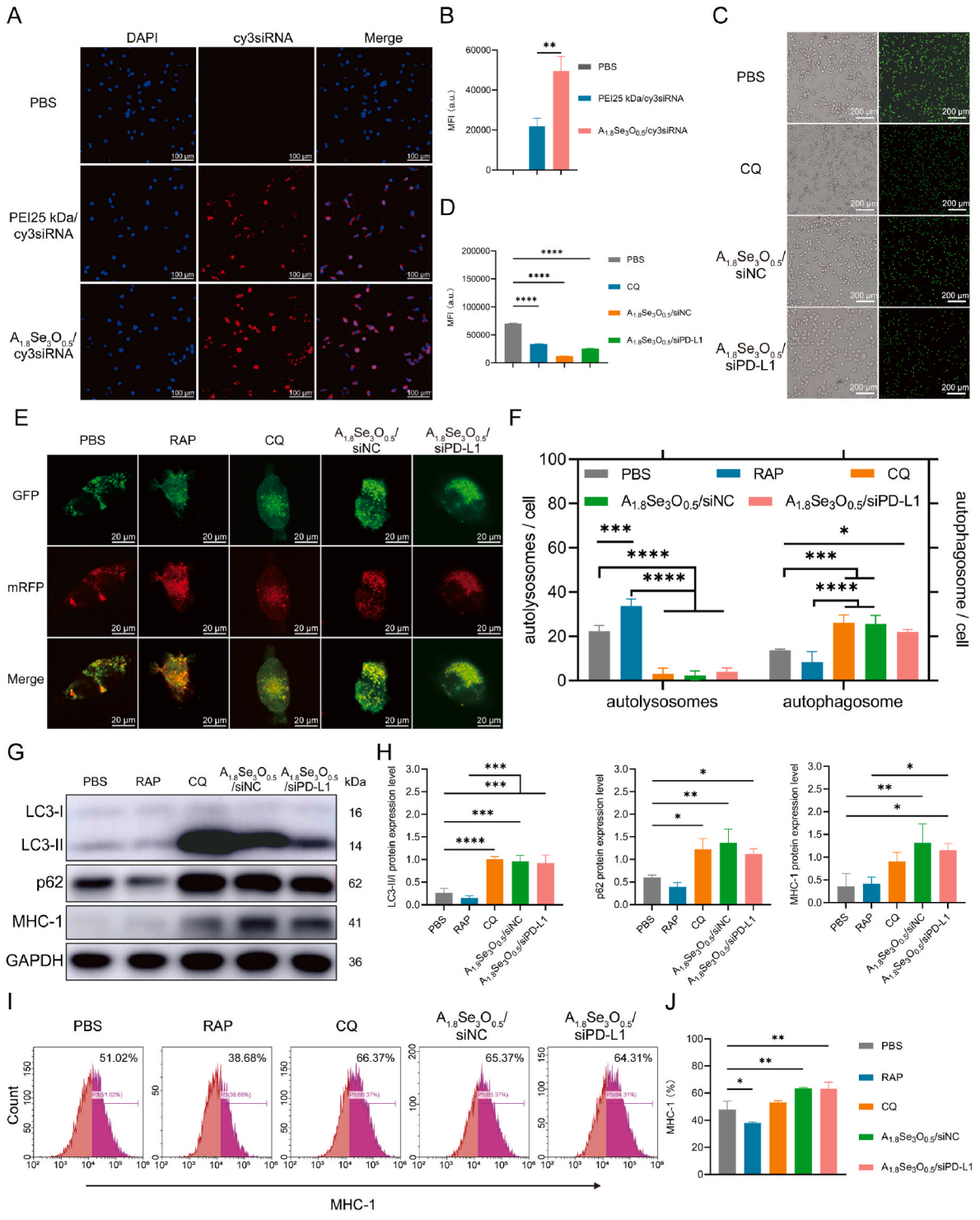

Fig. 3. $A_{1.8}Se_3O_{0.5}$/siPD-L1 alkalizes lysosomes, inhibits autophagy, and upregulates MHC-1 expression. (A) Comparison of cellular uptake rates between the product and PEI 25 kDa-labeled fluorescent siRNA. Scale bars = 100 μm. (B) Quantitative analysis of the cellular uptake efficiency of PEI 25 kDa/siRNA and $A_{1.8}Se_3O_{0.5}$/siRNA. (C) Fluorescence images of LysoSensor Green DND-189-stained MC38 cells. Scale bars = 200 μm. (D) Quantitative analysis of LysoSensor Green DND-189-stained MC38 cells. (E) and (F) Representative immunofluorescence images and quantitative analysis of the number of yellow autophagosomes and red autolysosomes among mRFP-GFP-LC3 puncta in MC38 cells. Scale bars = 20 μm. (G) Autophagy was detected by western blotting. (H) Semiquantitative analysis of the western blot data. (I) Flow cytometry analysis of MHC-1 expression in MC38 cells. (J) Quantitative analysis of flow cytometry data. The data are expressed as the mean ± SD (n = 3); $^*P < 0.05$, $^{**}P < 0.01$, $^{***}P < 0.001$.

inhibited autophagic flux by inducing lysosome alkalinization, as evidenced by the increased accumulation of autophagosomes and decreased accumulation of autolysosomes. Notably, the $A_{1.8}Se_3O_{0.5}$/siRNA nanogels were able to restore MHC-I expression in tumor cells. This is particularly significant because tumor cells often exhibit reduced MHC-I expression, which impairs antigen presentation and immune recognition [1]. The restoration of MHC-I expression by the nanogels suggests their potential for enhancing antigen presentation and improving immune responses against tumors.

2.4. $A_{1.8}Se_3O_{0.5}$/siPD-L1 effectively downregulated PD-L1 expression, leading to T-cell activation

The data presented thus far reveal a previously unreported link between PD-L1 and autophagy, indicating that autophagy blockade could lead to the upregulation of PD-L1 expression [56]. This upregulated PD-L1 exacerbates immunosuppression and immune tolerance within cancer cells, contributing to significant immune evasion [57]. To facilitate the knockdown of PD-L1 expression, PD-L1 siRNA was integrated into the nanogels to generate $A_{1.8}Se_3O_{0.5}$/siPD-L1. As anticipated, the protein expression of PD-L1 significantly increased in cells treated with $A_{1.8}Se_3O_{0.5}$/siNC, whereas $A_{1.8}Se_3O_{0.5}$/siPD-L1 markedly decreased the expression of PD-L1 (Fig. 4A and **B**). The role of $A_{1.8}Se_3O_{0.5}$ in this phenomenon was better demonstrated by treatment with free siPD-L1 as a control. Similar results were obtained through flow cytometry (Fig. 4C and **D**), RT−PCR analysis (Fig. S19), and immunofluorescence assays (Fig. S17). Overall, the PD-L1 protein and gene knockdown efficiencies were 56 % and 65 %, respectively, indicating that $A_{1.8}Se_3O_{0.5}$/siPD-L1 exhibits high efficacy in gene silencing.

Successful endosomal escape and release of siRNA into the cytoplasm are crucial prerequisites for effective siRNA delivery and subsequent knockdown of specific proteins [58]. Therefore, we verified the endosomal escape efficiency of $A_{1.8}Se_3O_{0.5}$/siPD-L1. To test this possibility, we used LysoTracker Green to stain lysosomes and Cy3-labeled siRNA to study the endosomal escape behavior of $A_{1.8}Se_3O_{0.5}$/siRNA in MC38 cells. As depicted in Fig. 4E, PEI25 kDa/cy3siRNA and $A_{1.8}Se_3O_{0.5}$/-cy3siRNA were incubated with MC38 cells for 6 h. The yellow fluorescence-stained dots indicate the overlap of Cy3-labeled siRNA-stained nanogels with LysoTracker Green-stained lysosomes. The overlap coefficient, defined as the area under the two probability density functions simultaneously, of PEI25 kDa/cy3siRNA was significantly greater than that of $A_{1.8}Se_3O_{0.5}$/siRNA, suggesting that the endosomal escape efficiency of $A_{1.8}Se_3O_{0.5}$/siPD-L1 was high (Fig. 4F). The exceptional endosomal escape efficiency of $A_{1.8}Se_3O_{0.5}$/siPD-L1 is largely attributed to the "proton sponge" effect of polyethyleneimine (PEI), a phenomenon that enhances the capacity of the drug to traverse the endosomal barrier. Additionally, endosomes contain a high concentration of reducing molecules, such as glutathione (GSH), or a high level of reactive oxygen species (ROS), which is significantly greater than that in the cytoplasm. GSH or ROS can promote the cleavage of diselenide bonds, thereby increasing the instability of nanogels [50,59]. The diselenide-cleaved complexes were postulated to be susceptible to dissociation when $A_{1.8}Se_3O_{0.5}$/siPD-L1 approached the negatively charged and lipophilic endosomal membrane, consequently eliciting TEM $A_{1.8}Se_3O_{0.5}$/siPD-L1 association with the endosomal membrane (due to electrostatic reactions and hydrophobic interactions) and the liberation of siRNA from the ruptured endosomal compartment. These findings underscore the promising application of $A_{1.8}Se_3O_{0.5}$/siPD-L1 in achieving ROS-mediated endosomal escape of nanogels, a critical step in enhancing the therapeutic efficacy of siRNA delivery systems [60–62]. In our investigation, we investigated the impact of PD-L1 downregulation on the activation of $CD8^+$ T cells. Tumor cells often exhibit high PD-L1 expression to reinforce the PD-1/PD-L1 pathway, leading to T-cell exhaustion and enabling tumor cells to evade immune surveillance [63,64]. By downregulating PD-L1 on cancer cells, we can potentially prevent the interaction between PD-1 and PD-L1, thereby reactivating the antitumor immune response of cytotoxic T cells [41]. Additionally, inhibiting autophagy could lead to an increase in MHC-I expression in tumor cells, ultimately enhancing antigen presentation and promoting antitumor T-cell responses [65]. Given these insights, we hypothesize that $A_{1.8}Se_3O_{0.5}$/siPD-L1 may activate the antitumor T-cell response through PD-L1 downregulation and MHC-I upregulation.

We evaluated the ability of $A_{1.8}Se_3O_{0.5}$/siPD-L1 to stimulate immune responses. First, to investigate the potential of $A_{1.8}Se_3O_{0.5}$/siPD-L1 in eliciting T-cell activation, we performed an OVA-specific T-cell assay using 5,6-carboxyfluorescein diacetate succinimidyl ester (CFSE) dilution (Fig. 4G). Initially, we immunized OT-1 mice with OVA peptide combined with Freund's complete adjuvant (CFA). After 21 days of immune stimulation, OVA-specific CTLs were isolated from the spleens of the mice and restimulated with OVA peptide and IL-2. These CTLs were then labeled with CFSE and cocultured with the MC38 cell line overexpressing OVA (MC38-OVA), which had been treated with either $A_{1.8}Se_3O_{0.5}$/siNC or $A_{1.8}Se_3O_{0.5}$/siPD-L1, to assess their proliferation. $A_{1.8}Se_3O_{0.5}$/siPD-L1-treated MC38-OVA cells exhibited robust T-cell proliferation (20 %), significantly surpassing the proliferation induced by $A_{1.8}Se_3O_{0.5}$/siNC-treated MC38-OVA cells (5.2 %) (Fig. 4H and **I**). These findings strongly suggest that $A_{1.8}Se_3O_{0.5}$/siPD-L1-treated cancer cells can efficiently induce T-cell activation. Subsequently, the ability of $A_{1.8}Se_3O_{0.5}$/siPD-L1 to activate and induce the maturation of spleen-derived dendritic cells was analyzed. After incubation with PBS, free siPD-L1, $A_{1.8}Se_3O_{0.5}$/siNC, or $A_{1.8}Se_3O_{0.5}$/siPD-L1 for 24 h, CD86 and CD80 expression on DCs was measured via flow cytometry. The expression of DC activation markers (CD80 and CD86) in both the $A_{1.8}Se_3O_{0.5}$/siNC and $A_{1.8}Se_3O_{0.5}$/siPD-L1 groups was significantly upregulated (Fig. S20). Encouraged by a good immune activation effect, we proceeded to assess the cytotoxic function of the activated splenic lymphocytes. The treated DCs were subsequently cocultured with splenic T cells. The T cells from each group were then harvested and cocultured with MC38 cells. The absorbance of the MC38 cells in the $A_{1.8}Se_3O_{0.5}$/siPD-L1 group was lower than that in the other groups (Fig. 4J), indicating a greater rate of cell death in the $A_{1.8}Se_3O_{0.5}$/siPD-L1 treatment group (Fig. 4K). Intriguingly, the observed cytotoxicity may not be solely attributed to the inhibition of PD-L1 and activation of DCs by $A_{1.8}Se_3O_{0.5}$/siPD-L1. The nanogel is capable of generating selenic acid under the influence of reactive oxygen species (ROS). Emerging evidence supports the significant antitumor potential of selenite, which can render tumor cells susceptible to NK cells. Gao et al. reported that the diselenide monomer DSeOH was noncytotoxic to DOX-resistant breast cancer cells (MCF-7-ADR) and triple-negative breast cancer cells (MDA-MB-231). However, the seleninic acid oxidation product RSeOOH had a marked antitumor effect. The strategy of Pan et al. to use seleninic acid and cetuximab in combination therapy opens a new avenue to improve the therapeutic effect of NK cell-based immunotherapy. Li et al. reported that diselenide bonds can be cleaved to form seleninic acid under 5 Gy of g-radiation, which activates cancer immunity in NK cells by inhibiting the expression of the HLA-E protein. Similarly, Xianyu et al. reported that intracellular ROS oxidize diselenide bonds in nanocomplexes to seleninic acid, which blocks the expression of another checkpoint receptor, human leukocyte antigen E. This multifaceted approach underscores the therapeutic potential of $A_{1.8}Se_3O_{0.5}$/siPD-L1 in modulating the immune response and enhancing the susceptibility of tumor cells to immune-mediated clearance [66–70].

Our study revealed a previously unreported connection between PD-L1 and autophagy, shedding light on how autophagy blockade can upregulate PD-L1 expression. By integrating PD-L1 siRNA into $A_{1.8}Se_3O_{0.5}$/siPD-L1 nanogels, we effectively achieved PD-L1 downregulation and demonstrated high endosomal escape efficiency. Moreover, our findings indicate that $A_{1.8}Se_3O_{0.5}$/siPD-L1 treatment can induce T-cell activation, suggesting its potential for enhancing antitumor immune responses. These discoveries offer valuable insights into the intricate interplay between PD-L1, autophagy, and immune evasion in cancer. The $A_{1.8}Se_3O_{0.5}$/siPD-L1 nanogels show promise as a therapeutic approach to counter immune suppression and bolster antitumor immunity. Further research is warranted to evaluate the in vivo efficacy and safety of $A_{1.8}Se_3O_{0.5}$/siPD-L1, bringing us closer to developing innovative immunotherapeutic strategies targeting PD-L1 and autophagy for cancer treatment.

2.5. Tissue distribution and antitumor activity of $A_{1.8}Se_3O_{0.5}$/siPD-L1

To investigate the distribution of $A_{1.8}Se_3O_{0.5}$/Cy5.5 siRNA in tumor-bearing mice, we utilized an MC38 tumor model and administered

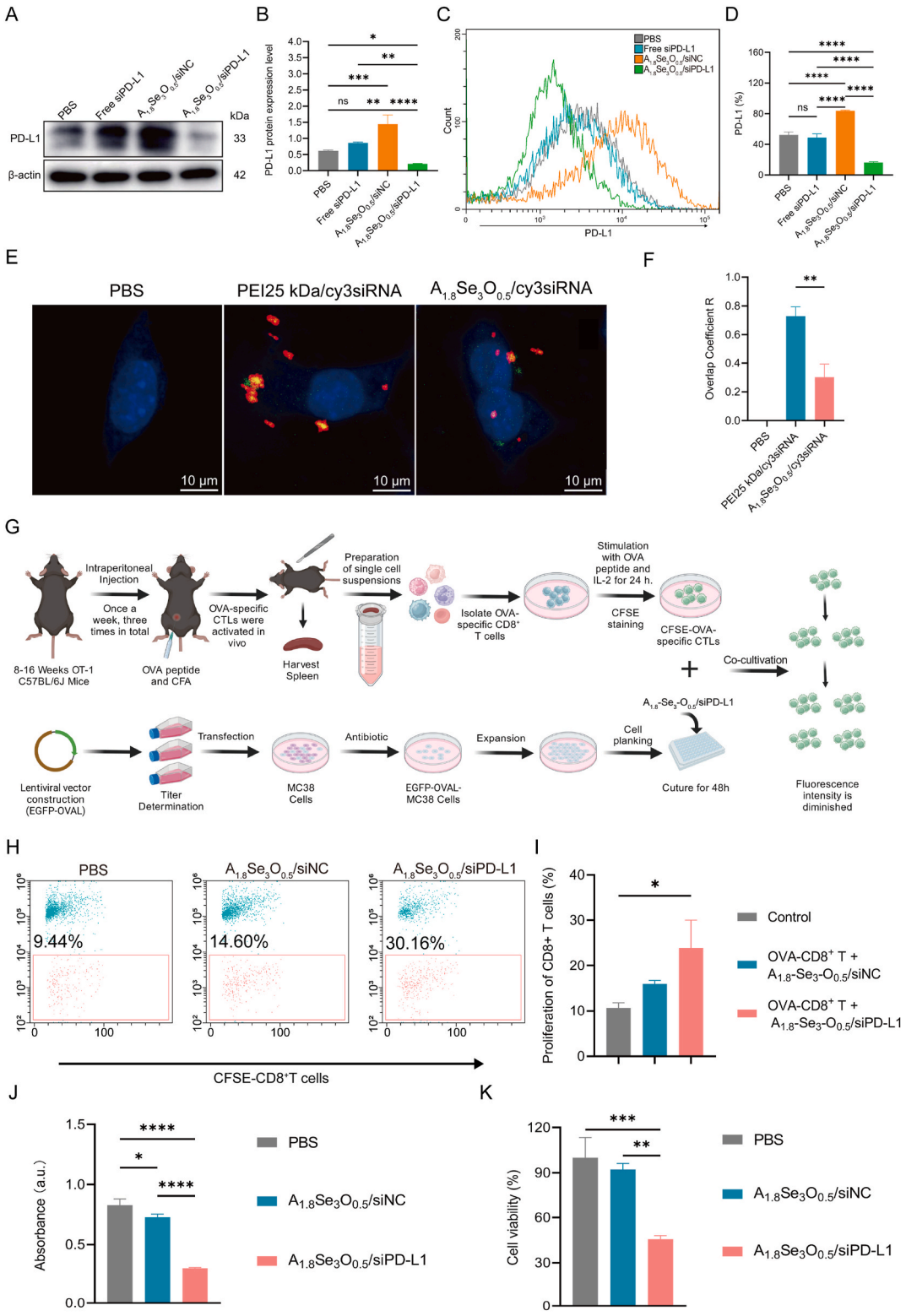

Fig. 4. $A_{1.8}Se_3O_{0.5}$/siPD-L1 inhibits autophagy and downregulates PD-L1 to activate $CD8^+$ T cells. (A) Validation of PD-L1 protein expression by Western blot. (B) Semiquantitative analysis of the Western blot data. (C) Flow cytometry analysis of PD-L1 expression in $A_{1.8}Se_3O_{0.5}$/siNC- or siPD-L1-treated MC38 cells. (D) Quantitative analysis of flow cytometry data. (E) Confocal images of endosomal disruption of MC38 cells cultured with $A_{1.8}Se_3O_{0.5}$/cy3siRNA and PEI 25 kDa/Cy3siRNA for 6 h siRNA (red) was labeled with Cy3, and lysosomes were dyed green with LysoGreen. Scale bar = 10 μm. (F) The degree of colocalization of red (Cy3 siRNA) and green (LysoGreen-stained lysosomes) fluorescence was determined using the overlap coefficient R calculated from the confocal images in E. (G) Schematic illustrating the in vitro proliferation study of OVA-specific CTLs coincubated with OVA-MC38 cells after PD-L1 knockdown. (H) MC38 cells transfected with $A_{1.8}Se_3O_{0.5}$/siPD-L1 were cocultured with CFSE-labeled OVA-specific $CD8^+$ T cells for 3 days. CTL proliferation was examined via flow cytometry analysis. (I) Quantitative analysis of flow cytometry data. (J) The absorbance of MC38 cells after they were killed by CTLs. (K) Cell viability of MC38 cells after killing by CTLs. The data are expressed as the mean ± SD (n = 3); $^*P < 0.05$, $^{**}P < 0.01$, $^{***}P < 0.001$.

$A_{1.8}Se_3O_{0.5}$/Cy5.5 siRNA intratumorally. Fig. 5A shows that the cumulative fluorescence intensity in the tumor increased over time, peaking at 6 h postinjection. The fluorescence intensities in the tumors of the $A_{1.8}Se_3O_{0.5}$/Cy5.5 siRNA-treated animals were significantly greater than those in the tumors of the naked siRNA-treated animals. This finding suggested that the nanogels efficiently accumulated at the tumor site and that abundant siRNAs escaped from the endosome and lysosome, were released from the polyplexes, and entered cancer cells. This finding was further supported by the semiquantitative analysis shown in Fig. 5B. This effect reduced the elimination of $A_{1.8}Se_3O_{0.5}$/Cy5.5 siRNA complexes from tumor tissues to the circulation and kidneys, especially at the early stage after injection, which in turn enhanced their accumulation and retention at the local site. Analysis of tissues collected at 6 h postinjection revealed that $A_{1.8}Se_3O_{0.5}$/Cy5.5 siRNA was predominantly distributed in tumors and kidneys, and no or very weak signals were detected in the spleen, lung or liver. The fluorescence signal in kidneys treated with free Cy5.5 siRNA was weaker than that in kidneys treated with $A_{1.8}Se_3O_{0.5}$/Cy5.5 siRNA (Fig. 5C and D), which was attributed to the much faster elimination of free siRNA from the body than from the polyplexes. To confirm the enhanced accumulation of $A_{1.8}Se_3O_{0.5}$/Cy5.5 siRNA in tumor tissues, we examined frozen sections of tumor tissues using fluorescence microscopy. The $A_{1.8}Se_3O_{0.5}$/Cy5.5 siRNA group exhibited greater fluorescence accumulation than the free Cy5.5 siRNA group (Fig. 5E and **F**). These results demonstrated the superior tumor accumulation of $A_{1.8}Se_3O_{0.5}$/Cy5.5 siRNA, laying a strong foundation for subsequent treatment efforts.

The antitumor efficacy of $A_{1.8}Se_3O_{0.5}$/siPD-L1 was evaluated in C57BL/6J tumor-bearing mice (Fig. 5G). After 10 days, after the subcutaneous inoculation of MC38 cells, the tumor volume reached 100 mm^3. Subsequently, $A_{1.8}Se_3O_{0.5}$/siPD-L1 was administered a total of 8 times (twice a week). Throughout the treatment, the mice did not exhibit any signs of overt toxicity, as evidenced by the absence of changes in body weight and behavior (Fig. 5K). Additionally, histological examination of the heart, liver, spleen, lung, and kidney revealed no significant organ damage in any of the groups (Fig. S21). As shown in Fig. 5H, **J**, and **5I**, treatment with the $A_{1.8}Se_3O_{0.5}$/siNC nanogels minimally suppressed tumor growth, whereas treatment with the $A_{1.8}Se_3O_{0.5}$/siPD-L1 nanogels significantly inhibited tumor growth, achieving a suppression rate of 69.5 %. These findings collectively indicate that the combination of $A_{1.8}Se_3O_{0.5}$ with PD-L1 effectively enhances antitumor efficacy. H&E-stained tumor sections revealed increased numbers of necrotic and apoptotic tumor cells and decreased Ki67 staining in the $A_{1.8}Se_3O_{0.5}$/siPD-L1 group (Fig. 5L and M, and 5 N).

The results demonstrated the efficient biodistribution and tumor accumulation of $A_{1.8}Se_3O_{0.5}$/Cy5.5 siRNA in an MC38 tumor-bearing mouse model. Furthermore, treatment with $A_{1.8}Se_3O_{0.5}$/siPD-L1 significantly suppressed tumor growth. Overall, the results highlight the potential of $A_{1.8}Se_3O_{0.5}$/siPD-L1 for targeted drug delivery and the downregulation of PD-L1 as a promising strategy for enhancing antitumor immune responses.

2.6. Mechanistic analysis of $A_{1.8}Se_3O_{0.5}$/siPD-L1 for in vivo antitumor assays

To gain a more comprehensive understanding of the impact of $A_{1.8}Se_3O_{0.5}$/siPD-L1 on tumor immunity, a multicolor immunofluorescence system was used to simultaneously monitor changes in various immune cell populations. CD4 and CD8 (T cells), Granzyme B, and PD-L1 were utilized as markers for this analysis. Representative fluorescence images (Fig. 6A) were quantified for each selected marker. Quantitative analysis of signal intensities revealed significant differences in immune cell counts among tumors treated with PBS, $A_{1.8}Se_3O_{0.5}$/siNC, or $A_{1.8}Se_3O_{0.5}$/siPD-L1 (Fig. 6B). Notably, $A_{1.8}Se_3O_{0.5}$/siPD-L1-treated tumors exhibited overall increases in the numbers of T cells and Granzyme B.

Subsequently, the effects of $A_{1.8}Se_3O_{0.5}$/siPD-L1 on autophagic flux, MHC-I expression, and PD-L1 fluctuations in vivo were investigated. In vivo experiments were also conducted to assess the impact of $A_{1.8}Se_3O_{0.5}$/siPD-L1 on autophagic flux, MHC-1 expression, and PD-L1 expression. Immunohistochemistry (IHC) analysis of LC3B and P62 expression revealed significantly greater staining intensity in the $A_{1.8}Se_3O_{0.5}$ group than in the PBS-treated group (Fig. 7A and **B**). Notably, the $A_{1.8}Se_3O_{0.5}$ group exhibited a 2-3-fold increase in staining intensity (Fig. 7C and **D**). Immunoblotting analysis further confirmed the ability of $A_{1.8}Se_3O_{0.5}$ to increase the LC3-II/I ratio, increase p62 accumulation, and increase MHC-1 and PD-L1 expression (Fig. 7E and **F**). Importantly, the combination of $A_{1.8}Se_3O_{0.5}$ with siPD-L1 resulted in decreased PD-L1 protein levels in tumor tissue (Fig. 7E and **F**). These findings provide additional evidence of the multifaceted effects of $A_{1.8}Se_3O_{0.5}$/siPD-L1 in modulating autophagy, MHC-1 expression, and PD-L1 levels within the tumor microenvironment.

To better understand the mechanisms underlying $A_{1.8}Se_3O_{0.5}$/siPD-L1 immunotherapy, we utilized flow cytometry analysis to examine the immune profiles of the tumor-draining lymph nodes (TDLNs) and the tumor microenvironment. Lymphocytes in the TDLN are essential for initiating immune responses, with mature dendritic cells (DCs) serving as the main antigen-presenting cells (APCs) [5,71]. Our results demonstrated that $A_{1.8}Se_3O_{0.5}$ effectively increased the frequency of $CD11c^+CD80^+$ dendritic cells and $CD11c^+CD86^+$ dendritic cells in the TDLN, reaching 2- to 3-fold greater levels than those in the PBS group (Fig. 7G and **H**). This finding suggested that $A_{1.8}Se_3O_{0.5}$ promotes the maturation of DCs in TDLNs. Furthermore, immune cells within the tumor microenvironment play vital roles in antitumor activity. To investigate the impact of $A_{1.8}Se_3O_{0.5}$/siPD-L1 on tumor immune escape, we analyzed the immune profiles of tumor tissues using flow cytometry [72,73]. As depicted in Fig. 7I and J, $A_{1.8}Se_3O_{0.5}$/siPD-L1 treatment significantly enhanced the infiltration of $CD4^+$ and $CD8^+$ T cells, particularly $CD8^+$ T cells, into tumors, exhibiting an approximately 2.4-fold increase compared to that in the PBS control group. Moreover, $A_{1.8}Se_3O_{0.5}$/siNC slightly induced the infiltration of $CD8^+$ T cells into the tumor (Fig. 7J). We also evaluated the expression of Granzyme B, a serine protease secreted by CTLs that induces tumor cell apoptosis. Flow cytometry analysis revealed that $A_{1.8}Se_3O_{0.5}$/siPD-L1 significantly facilitated the recruitment of granzyme B, which was approximately 5-fold greater than that in the PBS group and $A_{1.8}Se_3O_{0.5}$/siNC group (Fig. 7K). These findings shed light on the mechanisms by which $A_{1.8}Se_3O_{0.5}$/siPD-L1 immunotherapy modulates the immune landscape, promotes the maturation of DCs and enhances the recruitment of $CD8^+$ T cells and granzyme B to the tumor microenvironment.

In summary, these results provide valuable insights into the mechanisms of $A_{1.8}Se_3O_{0.5}$/siPD-L1-induced immunotherapy. We observed changes in immune cell populations and markers associated with tumor immunity. In TDLNs, $A_{1.8}Se_3O_{0.5}$ treatment increased the percentage of $CD11c^+CD80^+$ and $CD11c^+CD86^+$ DCs, indicating a stronger DC-based immune response in TDLNs. In the tumor microenvironment, $A_{1.8}Se_3O_{0.5}$/siPD-L1 treatment increased the frequency of $CD4^+$ and $CD8^+$ T cells, particularly $CD8^+$ T cells, suggesting that enhanced antitumor activity was initiated by $A_{1.8}Se_3O_{0.5}$/siPD-L1. $A_{1.8}Se_3O_{0.5}$/siNC inhibited autophagy by disrupting lysosomal function and restoring MHC-I expression, whereas $A_{1.8}Se_3O_{0.5}$/siPD-L1 not only restored MHC-I expression but also effectively inhibited PD-L1 expression, resulting in the effective prevention of immune escape by effectively promoting DC maturation and recruitment of $CD8^+$ T cells.

3. Conclusion

In conclusion, our study successfully developed a straightforward combinatorial selenol chemistry strategy to produce a diverse library of diselenide-crosslinked cationic nanogels for siRNA delivery. Through a rigorous high-throughput screening process, we identified the $A_{1.8}Se_3O_{0.5}$ nanogels as the optimal candidates for efficient delivery of PD-L1 siRNA. These nanogels exhibited enhanced internalization by

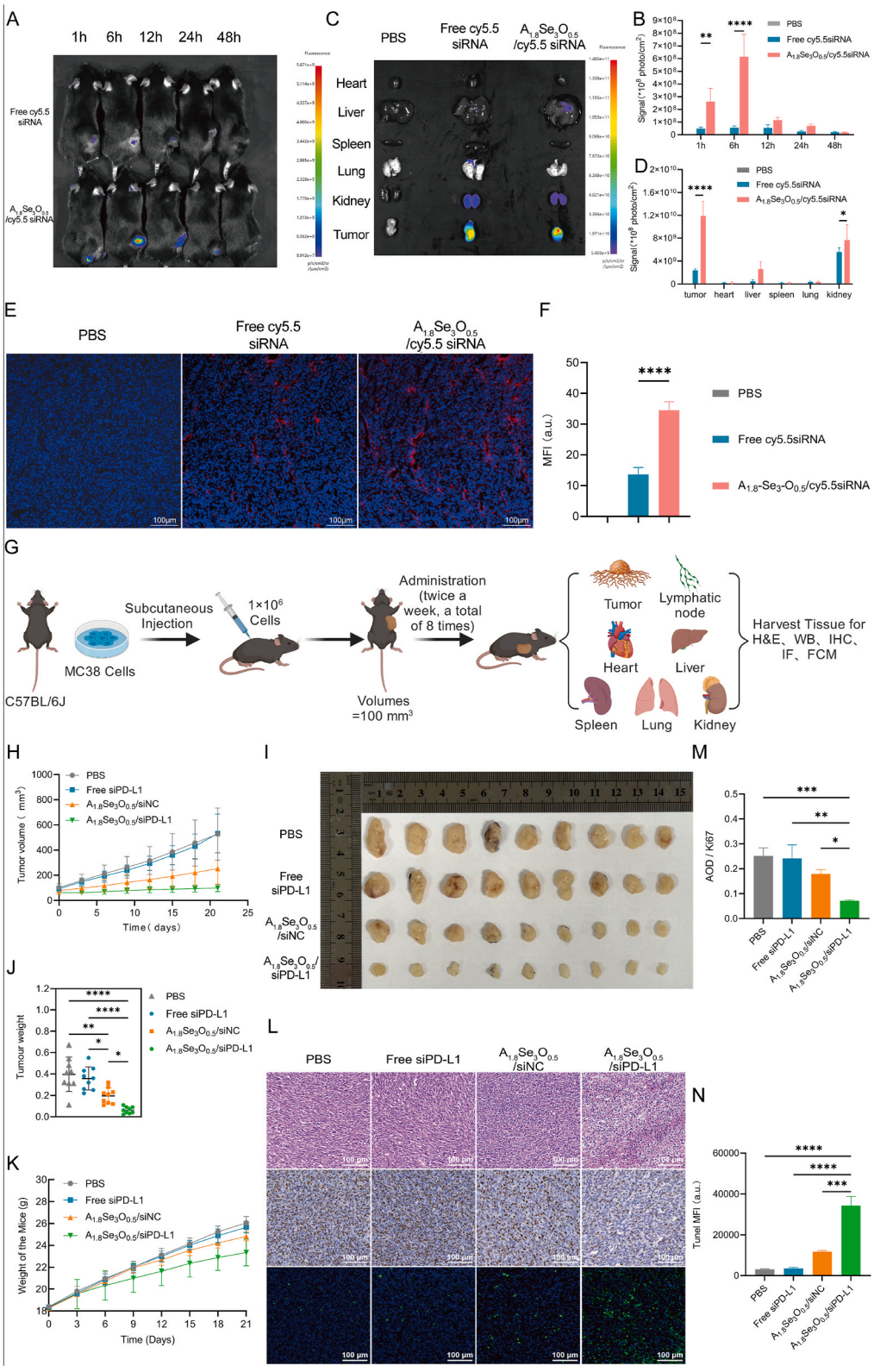

Fig. 5. In vivo and in vitro experiments were conducted to evaluate the infiltration and antitumor effects of $A_{1.8}Se_3O_{0.5}$/siPD-L1. (A, B) The distribution of $A_{1.8}Se_3O_{0.5}$/Cy5.5 siRNA and free Cy5.5 siRNA in MC38 tumor-bearing mice was assessed at 1 h, 6 h, 12 h, 24 h, and 48 h postadministration. (C, D) Major organs and tumors in mice were isolated and imaged, and their mean fluorescence intensity was quantified. (E, F) Frozen sections of tumor tissues were examined via fluorescence microscopy. (G) A schematic diagram depicting the process of constructing C57BL/6J tumor-bearing mice. (H) Tumor growth curves following treatment with various therapeutics. (I, J, K) Images of tumors (I), tumor weights (J), and weights of mice (K) following various treatments. (L, M, N) H&E, Ki67, and TUNEL analyses of tumor tissues were also conducted. Scale bars = 100 μm. The data are expressed as the mean ± SD. (B), (D), (F), (M) and (N), n = 3; (H–K), n = 9; $^*P < 0.05$, $^{**}P < 0.01$, $^{***}P < 0.001$.

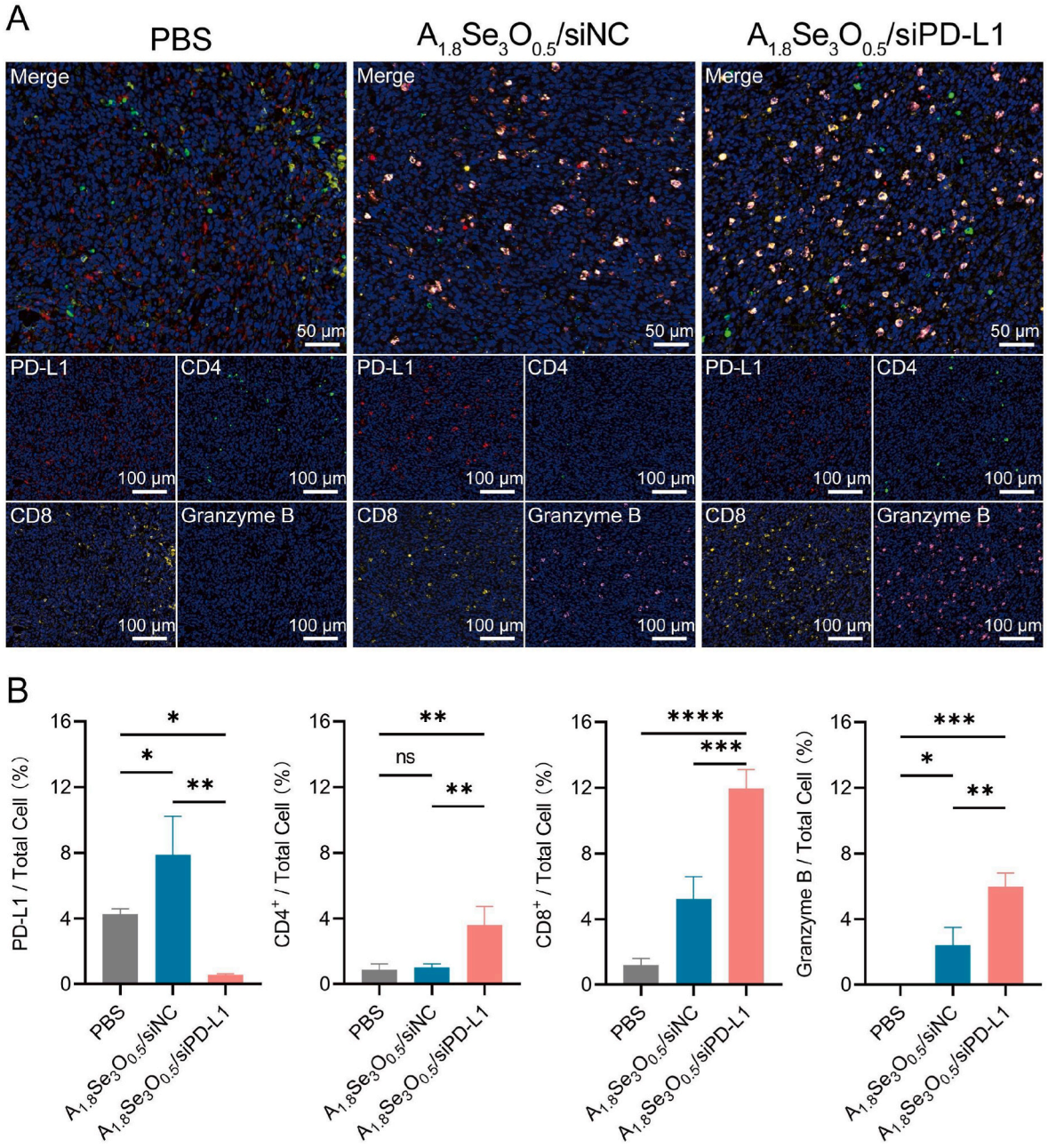

Fig. 6. Multicolor immunofluorescence analysis revealed that the tumor immune microenvironment was modulated by $A_{1.8}Se_3O_{0.5}$/siPD-L1. Specific IF images of PBS-treated tumors and $A_{1.8}Se_3O_{0.5}$/siNC- and $A_{1.8}Se_3O_{0.5}$/siPD-L1-treated tumors (A) and quantitation of the markers shown in A (n = 3 for each group) (B). Scale bars = 50 or 100 μm. The data are expressed as the mean ± SD (n = 3); $^*P < 0.05$, $^{**}P < 0.01$, $^{***}P < 0.001$.

tumor cells and demonstrated exceptional oxidative degradation capacity, leading to the inhibition of autophagy through lysosomal alkalinization. Importantly, the $A_{1.8}Se_3O_{0.5}$/siPD-L1 nanogels significantly reduced PD-L1 expression and increased the level of major histocompatibility complex class I (MHC-I), resulting in enhanced proliferation of specific $CD8^+$ T cells and slowed MC38 tumor growth. Consequently, the $A_{1.8}Se_3O_{0.5}$/siPD-L1 nanogels effectively restrained tumor growth through autophagy inhibition, upregulation of MHC-I, and downregulation of PD-L1. Thus, these nanogels, which incorporate dynamic diselenide bonds, demonstrated potential for synergistic antitumor efficacy by simultaneously inhibiting autophagy and preventing immune evasion. We anticipate that the facile and generalizable combinatorial reaction functionalization methodology described in this study can be extended to a wide range of cationic polymers with primary, secondary, and tertiary amine groups, opening up new avenues for the development of nanogel-based gene therapeutics.

Ethics approval and consent to participate

All the protocols for animal experiments were approved by the Shanghai Changhai Hospital Ethics Committee (No. CHEC(A.E)2023-006).

CRediT authorship contribution statement

Jie Gao: Writing – review & editing, Funding acquisition, Conceptualization. **Yonghua Zhai:** Writing – original draft, Methodology. **Weihong Lu:** Writing – original draft, Formal analysis, Data curation. **Xianghe Jiang:** Data curation. **Jingsheng Zhou:** Data curation. **Lili Wu:** Validation. **Longhai Du:** Data curation. **Chunqing Ou:** Writing –

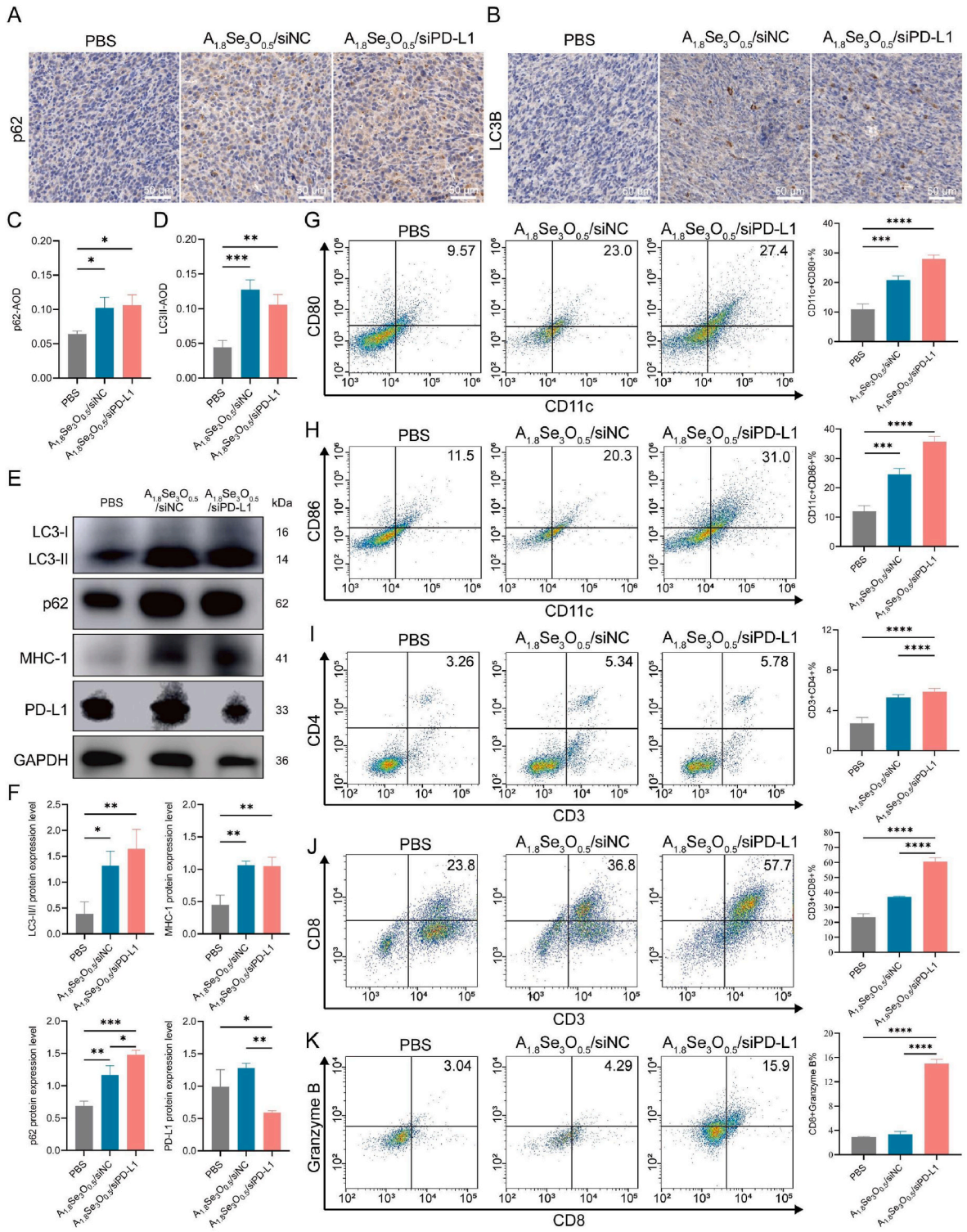

Fig. 7. The effects of $A_{1.8}Se_3O_{0.5}$/siPD-L1 on immune cells and tumor cells in the tumor environment. IHC analysis to determine p62 (A) and LC3B (B) expression at the orthotopic tumor site. Quantitative assessment of p62 (C) and LC3B (D) release. (E) The treated tumor tissue was subjected to further analysis via LC3-II/I, p62, PD-L1 and MHC-1 immunoblotting. (F) ImageJ software was used to quantify the band density. (G) and (H) Representative flow cytometry plots and quantitative analysis of mature DCs ($CD11c^+CD80^+$ and $CD11c^+CD86^+$) in TDLNs. (I), (J) and (K) Representative flow cytometry plots and quantitative analysis of $CD3^+CD4^+$, $CD3^+CD8^+$ and $CD8^+$Granzyme B^+ T cells in tumors. Scale bars = 50 μm. The data are expressed as the mean ± SD (n = 3); $^*P < 0.05$, $^{**}P < 0.01$, $^{***}P < 0.001$.

original draft. **Xinyi Zhang:** Visualization. **Hanliang He:** Investigation. **Jian Zhu:** Resources. **Zhengbiao Zhang:** Supervision, Resources. **Meiyun Li:** Formal analysis. **Yan Wu:** Writing – original draft, Resources. **Xiangqiang Pan:** Writing – review & editing, Supervision, Project administration, Funding acquisition, Conceptualization.

Declaration of competing interest

The authors do not have any conflicts of interest to declare.

Acknowledgments

This work was supported by the National Natural Science Foundation of China (No. 21971177, 82072051), the Natural Science Foundation of the Jiangsu Higher Education Institution of China (No. 22KJA150004), the Priority Academic Program Development (PAPD) of Jiangsu Higher Education Institutions, the Jiangsu Key Laboratory of Advanced Functional Polymers Design and Application, Soochow University, and the Suzhou Key Laboratory of Macromolecular Design and Precision Synthesis and the Program of Innovative Research Team of Soochow University.

Appendix A. Supplementary data

Supplementary data to this article can be found online at https://doi.org/10.1016/j.bioactmat.2024.08.013.

References

[1] K. Yamamoto, A. Venida, J. Yano, D.E. Biancur, M. Kakiuchi, S. Gupta, A.S. W. Sohn, S. Mukhopadhyay, E.Y. Lin, S.J. Parker, R.S. Banh, J.A. Paulo, K.W. Wen, J. Debnath, G.E. Kim, J.D. Mancias, D.T. Fearon, R.M. Perera, A.C. Kimmelman, Autophagy promotes immune evasion of pancreatic cancer by degrading MHC-I, Nature 581 (7806) (2020) 100–105.

[2] K. Yamamoto, A. Venida, R.M. Perera, A.C. Kimmelman, Selective autophagy of MHC-I promotes immune evasion of pancreatic cancer, Autophagy 16 (8) (2020) 1524–1525.

[3] J.M.M. Levy, C.G. Towers, A. Thorburn, Targeting autophagy in cancer, Nat. Rev. Cancer 17 (9) (2017) 528–542.

[4] H. Xia, D.R. Green, W. Zou, Autophagy in tumour immunity and therapy, Nat. Rev. Cancer 21 (5) (2021) 281–297.

[5] S. Zhang, F. Xie, K. Li, H. Zhang, Y. Yin, Y. Yu, G. Lu, S. Zhang, Y. Wei, K. Xu, Y. Wu, H. Jin, L. Xiao, L. Bao, C. Xu, Y. Li, Y. Lu, J. Gao, Gold nanoparticle-directed autophagy intervention for antitumor immunotherapy via inhibiting tumor-associated macrophage M2 polarization, Acta Pharm. Sin. B 12 (7) (2022) 3124–3138.

[6] H. Abeliovich, J. Debnath, W.X. Ding, W.T. Jackson, D.H. Kim, D.J. Klionsky, N. Ktistakis, M. Margeta, C. Munz, M. Petersen, J. Sadoshima, I. Vergne, Where is the field of autophagy research heading? Autophagy 19 (4) (2023) 1049–1054.

[7] T.M.H. Nguyen, S.G. Shin, H.W. Choi, C.W. Bark, Recent advances in self-powered and flexible UVC photodetectors, Exploration (Beijing) 2 (5) (2022) 20210078.

[8] X. Wang, W.K.K. Wu, J. Gao, Z. Li, B. Dong, X. Lin, Y. Li, Y. Li, J. Gong, C. Qi, Z. Peng, J. Yu, L. Shen, Autophagy inhibition enhances PD-L1 expression in gastric cancer, J. Exp. Clin. Cancer Res. 38 (1) (2019) 140.

[9] E. Philipson, C. Engstrom, P. Naredi, J. Bourghardt Fagman, High expression of p62/SQSTM1 predicts shorter survival for patients with pancreatic cancer, BMC Cancer 22 (1) (2022) 347.

[10] X. Liu, J. Jiang, Y.P. Liao, I. Tang, E. Zheng, W. Qiu, M. Lin, X. Wang, Y. Ji, K. C. Mei, Q. Liu, C.H. Chang, Z.A. Wainberg, A.E. Nel, H. Meng, Combination chemo-immunotherapy for pancreatic cancer using the immunogenic effects of an irinotecan silicasome nanocarrier plus anti-PD-1, Adv. Sci. 8 (6) (2021) 2002147.

[11] H. Huang, C. Dong, M. Chang, L. Ding, L. Chen, W. Feng, Y. Chen, Mitochondria-specific nanocatalysts for chemotherapy-augmented sequential chemoreactive tumor therapy, Exploration (Beijing) 1 (1) (2021) 50–60.

[12] Y. Xu, G. Song, S. Xie, W. Jiang, X. Chen, M. Chu, X. Hu, Z.W. Wang, The roles of PD-1/PD-L1 in the prognosis and immunotherapy of prostate cancer, Mol. Ther. 29 (6) (2021) 1958–1969.

[13] L. Booth, J.L. Roberts, A. Poklepovic, P. Dent, [pemetrexed + sildenafil], via autophagy-dependent HDAC downregulation, enhances the immunotherapy response of NSCLC cells, Cancer Biol. Ther. 18 (9) (2017) 705–714.

[14] H. Chang, Z. Zou, Targeting autophagy to overcome drug resistance: further developments, J. Hematol. Oncol. 13 (1) (2020) 159.

[15] C.W. Lin, M.S. Jan, J.H. Kuo, Autophagy-related gene expression analysis of wild-type and atg5 gene knockout mouse embryonic fibroblast cells treated with polyethylenimine, Mol. Pharm. 11 (9) (2014) 3002–3008.

[16] X. Gao, L. Yao, Q. Song, L. Zhu, Z. Xia, H. Xia, X. Jiang, J. Chen, H. Chen, The association of autophagy with polyethylenimine-induced cytotoxicity in nephritic and hepatic cell lines, Biomaterials 32 (33) (2011) 8613–8625.

[17] S. Uchida, C.Y.J. Lau, M. Oba, K. Miyata, Polyplex designs for improving the stability and safety of RNA therapeutics, Adv. Drug Deliv. Rev. 199 (2023) 114972.

[18] R. Kumar, C.F. Santa Chalarca, M.R. Bockman, C.V. Bruggen, C.J. Grimme, R. J. Dalal, M.G. Hanson, J.K. Hexum, T.M. Reineke, Polymeric delivery of therapeutic nucleic acids, Chem. Rev. 121 (18) (2021) 11527–11652.

[19] C. Wang, Z. Li, P. Xu, L. Xu, S. Han, Y. Sun, Combination of polythyleneimine regulating autophagy prodrug and Mdr1 siRNA for tumor multidrug resistance, J. Nanobiotechnol. 20 (1) (2022) 476.

[20] O. Boussif, F. Lezoualc'h, M.A. Zanta, M.D. Mergny, D. Scherman, B. Demeneix, J. P. Behr, A versatile vector for gene and oligonucleotide transfer into cells in culture and in vivo: polyethylenimine, Proc. Natl. Acad. Sci. U. S. A. 92 (16) (1995) 7297–7301.

[21] O.F. Khan, P.S. Kowalski, J.C. Doloff, J.K. Tsosie, V. Bakthavatchalu, C.B. Winn, J. Haupt, M. Jamiel, R. Langer, D.G. Anderson, Endothelial siRNA delivery in nonhuman primates using ionizable low-molecular weight polymeric nanoparticles, Sci. Adv. 4 (6) (2018) eaar8409.

[22] A. Ishaqat, A. Herrmann, Polymers strive for accuracy: from sequence-defined polymers to mRNA vaccines against COVID-19 and polymers in nucleic acid therapeutics, J. Am. Chem. Soc. 143 (49) (2021) 20529–20545.

[23] P. Huang, H. Deng, Y. Zhou, X. Chen, The roles of polymers in mRNA delivery, Matter 5 (6) (2022) 1670–1699.

[24] J. Wang, H. He, X. Xu, X. Wang, Y. Chen, L. Yin, Far-red light-mediated programmable anti-cancer gene delivery in cooperation with photodynamic therapy, Biomaterials 171 (2018) 72–82.

[25] B. Kalyanaraman, G. Cheng, M. Hardy, O. Ouari, B. Bennett, J. Zielonka, Teaching the basics of reactive oxygen species and their relevance to cancer biology: mitochondrial reactive oxygen species detection, redox signaling, and targeted therapies, Redox Biol. 15 (2018) 347–362.

[26] H. Peng, F. Yao, J. Zhao, W. Zhang, L. Chen, X. Wang, P. Yang, J. Tang, Y. Chi, Unraveling mitochondria-targeting reactive oxygen species modulation and their implementations in cancer therapy by nanomaterials, Exploration (Beijing) 3 (2) (2023) 20220115.

[27] D. Jana, Y. Zhao, Strategies for enhancing cancer chemodynamic therapy performance, Exploration (Beijing) 2 (2) (2022) 20210238.

[28] J. Liu, Y. Zhou, Q. Lyu, X. Yao, W. Wang, Targeted protein delivery based on stimuli-triggered nanomedicine, Exploration (Beijing) 4 (3) (2024) 20230025.

[29] X. Liu, J. Xiang, D. Zhu, L. Jiang, Z. Zhou, J. Tang, X. Liu, Y. Huang, Y. Shen, Fusogenic reactive oxygen species triggered charge-reversal vector for effective gene delivery, Adv. Mater. 28 (9) (2016) 1743–1752.

[30] M.S. Shim, Y. Xia, A reactive oxygen species (ROS)-responsive polymer for safe, efficient, and targeted gene delivery in cancer cells, Angew Chem. Int. Ed. Engl. 52 (27) (2013) 6926–6929.

[31] J. Wang, X. He, S. Shen, Z. Cao, X. Yang, ROS-sensitive cross-linked polyethylenimine for red-light-activated siRNA therapy, ACS Appl. Mater. Interfaces 11 (2) (2019) 1855–1863.

[32] H.S. Slocumb, S. Nie, V.M. Dong, X.H. Yang, Enantioselective selenol-ene using Rh-hydride catalysis, J. Am. Chem. Soc. 144 (40) (2022) 18246–18250.

[33] V.R. Juneja, K.A. McGuire, R.T. Manguso, M.W. LaFleur, N. Collins, W.N. Haining, G.J. Freeman, A.H. Sharpe, PD-L1 on tumor cells is sufficient for immune evasion in immunogenic tumors and inhibits CD8 T cell cytotoxicity, J. Exp. Med. 214 (4) (2017) 895–904.

[34] M.A. Curran, W. Montalvo, H. Yagita, J.P. Allison, PD-1 and CTLA-4 combination blockade expands infiltrating T cells and reduces regulatory T and myeloid cells within B16 melanoma tumors, Proc. Natl. Acad. Sci. U. S. A. 107 (9) (2010) 4275–4280.

[35] W. Zou, J.D. Wolchok, L. Chen, PD-L1 (B7-H1) and PD-1 pathway blockade for cancer therapy: mechanisms, response biomarkers, and combinations, Sci. Transl. Med. 8 (328) (2016) 328rv4.

[36] Z.A. Cooper, V.R. Juneja, P.T. Sage, D.T. Frederick, A. Piris, D. Mitra, J.A. Lo, F. S. Hodi, G.J. Freeman, M.W. Bosenberg, M. McMahon, K.T. Flaherty, D.E. Fisher, A.H. Sharpe, J.A. Wargo, Response to BRAF inhibition in melanoma is enhanced when combined with immune checkpoint blockade, Cancer Immunol. Res. 2 (7) (2014) 643–654.

[37] X. Wang, S. Liu, Y. Sun, X. Yu, S.M. Lee, Q. Cheng, T. Wei, J. Gong, J. Robinson, D. Zhang, X. Lian, P. Basak, D.J. Siegwart, Preparation of selective organ-targeting (SORT) lipid nanoparticles (LNPs) using multiple technical methods for tissue-specific mRNA delivery, Nat. Protoc. 18 (1) (2023) 265–291.

[38] Z. Sun, C. Song, C. Wang, Y. Hu, J. Wu, Hydrogel-based controlled drug delivery for cancer treatment: a review, Mol. Pharm. 17 (2) (2020) 373–391.

[39] Y. Gao, Q. Ma, Bacterial infection microenvironment-responsive porous microspheres by microfluidics for promoting anti-infective therapy, Smart Med. 1 (1) (2022).

[40] X. Cao, L. Sun, Z. Luo, X. Lin, Y. Zhao, Aquaculture derived hybrid skin patches for wound healing, Eng. Regenerat. 4 (1) (2023) 28–35.

[41] S. Yang, F. Wang, H. Han, H.A. Santos, Y. Zhang, H. Zhang, J. Wei, Z. Cai, Fabricated technology of biomedical micro-nano hydrogel, Biomed. Technol. 2 (2023) 31–48.

[42] F. Lin, Y. Li, W. Cui, Injectable hydrogel microspheres in cartilage repair, Biomed. Technol. 1 (2023) 18–29.

[43] D. Zhang, W. Li, Y. Shang, L. Shang, Programmable microfluidic manipulations for biomedical applications, Eng. Regenerat. 3 (3) (2022) 258–261.

[44] Z. Shatsberg, X. Zhang, P. Ofek, S. Malhotra, A. Krivitsky, A. Scomparin, G. Tiram, M. Calderon, R. Haag, R. Satchi-Fainaro, Functionalized nanogels carrying an anticancer microRNA for glioblastoma therapy, J. Contr. Release 239 (2016) 159–168.

[45] M. Satpathy, R. Mezencev, L. Wang, J.F. McDonald, Targeted in vivo delivery of EGFR siRNA inhibits ovarian cancer growth and enhances drug sensitivity, Sci. Rep. 6 (2016) 36518.

[46] D. Zhang, S. Tian, Y. Liu, M. Zheng, X. Yang, Y. Zou, B. Shi, L. Luo, Near infrared-activatable biomimetic nanogels enabling deep tumor drug penetration inhibit orthotopic glioblastoma, Nat. Commun. 13 (1) (2022) 6835.

[47] L. Wang, K. Zhu, W. Cao, C. Sun, C. Lu, H. Xu, ROS-triggered degradation of selenide-containing polymers based on selenoxide elimination, Polym. Chem. 10 (16) (2019) 2039–2046.

[48] Y. Fang, X. Lin, X. Jin, D. Yang, S. Gao, K. Shi, M. Yang, Design and fabrication of dual redox responsive nanoparticles with diselenide linkage combined photodynamically to effectively enhance gene expression, Int. J. Nanomed. 15 (2020) 7297–7314.

[49] S. Raisin, M. Morille, C. Bony, D. Noel, J.M. Devoisselle, E. Belamie, Tripartite polyionic complex (PIC) micelles as non-viral vectors for mesenchymal stem cell siRNA transfection, Biomater. Sci. 5 (9) (2017) 1910–1921.
[50] Y. He, S. Guo, L. Wu, P. Chen, L. Wang, Y. Liu, H. Ju, Near-infrared boosted ROS responsive siRNA delivery and cancer therapy with sequentially peeled upconversion nano-onions, Biomaterials 225 (2019) 119501.
[51] S. Yang, K.H. Wong, P. Hua, C. He, H. Yu, D. Shao, Z. Shi, M. Chen, ROS-responsive fluorinated polyethyleneimine vector to co-deliver shMTHFD2 and shGPX4 plasmids induces ferroptosis and apoptosis for cancer therapy, Acta Biomater. 140 (2022) 492–505.
[52] A.V. Onorati, M. Dyczynski, R. Ojha, R.K. Amaravadi, Targeting autophagy in cancer, Cancer 124 (16) (2018) 3307–3318.
[53] M. Ala, M.R.F. Khoshdel, A.R. Dehpour, Empagliflozin enhances autophagy, mitochondrial biogenesis, and antioxidant defense and ameliorates renal ischemia/reperfusion in nondiabetic rats, Oxid. Med. Cell. Longev. 2022 (2022) 1197061.
[54] S.J. Jeong, X. Zhang, A. Rodriguez-Velez, T.D. Evans, B. Razani, p62/SQSTM1 and selective autophagy in cardiometabolic diseases, Antioxidants Redox Signal. 31 (6) (2019) 458–471.
[55] F. Zhou, J. Gao, Y. Tang, Z. Zou, S. Jiao, Z. Zhou, H. Xu, Z.P. Xu, H. Yu, Z. Xu, Engineering chameleon prodrug nanovesicles to increase antigen presentation and inhibit PD-L1 expression for circumventing immune resistance of cancer, Adv. Mater. 33 (43) (2021) e2102668.
[56] J.Y. Jung, H.J. Ryu, S.H. Lee, D.Y. Kim, M.J. Kim, E.J. Lee, Y.M. Ryu, S.Y. Kim, K. P. Kim, E.Y. Choi, H.J. Ahn, S. Chang, siRNA nanoparticle targeting PD-L1 activates tumor immunity and abrogates pancreatic cancer growth in humanized preclinical model, Cells 10 (10) (2021).
[57] P.Y. Teo, C. Yang, L.M. Whilding, A.C. Parente-Pereira, J. Maher, A.J. George, J. L. Hedrick, Y.Y. Yang, S. Ghaem-Maghami, Ovarian cancer immunotherapy using PD-L1 siRNA targeted delivery from folic acid-functionalized polyethylenimine: strategies to enhance T cell killing, Adv. Healthcare Mater. 4 (8) (2015) 1180–1189.
[58] H. Wang, X. Liu, X. Ai, K.C. Remant-Bahadur, T.A. Dick, B. Yan, T. Lu, X. Zhou, R. Luo, M. Liu, X. Wang, K. Li, W. Wang, H. Uludag, W. Fu, Safe and effective delivery of mRNA using modified PEI-based lipopolymers, Pharmaceutics 15 (2) (2023).
[59] Y. Zhai, L. Wu, J. Gao, J. Zhou, L. Du, X. Fu, Y. Gao, T. Zhang, M. Zhang, W. Lu, Y. Wu, ROS-sensitive selenium-containing cationic brush polymer with potent gene transfection efficiency and biocompatibility, J. Appl. Polym. Sci. 141 (14) (2024).
[60] R. Cheng, F. Feng, F. Meng, C. Deng, J. Feijen, Z. Zhong, Glutathione-responsive nano-vehicles as a promising platform for targeted intracellular drug and gene delivery, J. Contr. Release 152 (1) (2011) 2–12.
[61] H. Sun, F. Meng, R. Cheng, C. Deng, Z. Zhong, Reduction-responsive polymeric micelles and vesicles for triggered intracellular drug release, Antioxidants Redox Signal. 21 (5) (2014) 755–767.
[62] T. Kurz, J.W. Eaton, U.T. Brunk, Redox activity within the lysosomal compartment: implications for aging and apoptosis, Antioxidants Redox Signal. 13 (4) (2010) 511–523.
[63] W. Li, F. Wu, S. Zhao, P. Shi, S. Wang, D. Cui, Correlation between PD-1/PD-L1 expression and polarization in tumor-associated macrophages: a key player in tumor immunotherapy, Cytokine Growth Factor Rev. 67 (2022) 49–57.
[64] F.K. Dermani, P. Samadi, G. Rahmani, A.K. Kohlan, R. Najafi, PD-1/PD-L1 immune checkpoint: potential target for cancer therapy, J. Cell. Physiol. 234 (2) (2019) 1313–1325.
[65] J. Tu, H. Xu, L. Ma, C. Li, W. Qin, X. Chen, M. Yi, L. Sun, B. Liu, X. Yuan, Nintedanib enhances the efficacy of PD-L1 blockade by upregulating MHC-I and PD-L1 expression in tumor cells, Theranostics 12 (2) (2022) 747–766.
[66] B. Xianyu, S. Pan, S. Gao, H. Xu, T. Li, Selenium-containing nanocomplexes achieve dual immune checkpoint blockade for NK cell reinvigoration, Small 20 (19) (2024) e2306225.
[67] S. Pan, J. Guan, B. Xianyu, Y. Tan, T. Li, H. Xu, A nanotherapeutic strategy to reverse NK cell exhaustion, Adv. Mater. 35 (23) (2023) e2211370.
[68] S. Gao, T. Li, Y. Guo, C. Sun, B. Xianyu, H. Xu, Selenium-containing nanoparticles combine the NK cells mediated immunotherapy with radiotherapy and chemotherapy, Adv. Mater. 32 (12) (2020) e1907568.
[69] T. Li, S. Pan, S. Gao, W. Xiang, C. Sun, W. Cao, H. Xu, Diselenide-Pemetrexed assemblies for combined cancer immuno-, radio-, and chemotherapies, Angew Chem. Int. Ed. Engl. 59 (7) (2020) 2700–2704.
[70] S. Liu, N. Li, H. Lai, L. Xu, Y. Zeng, X. Chen, H. Huang, T. Chen, J. Liu, J. Wang, Selenium nanoparticles enhance NK cell-mediated tumoricidal activity in malignant pleural effusion via the TrxR1-IL-18RAP-pSTAT3 pathway, Adv. Funct. Mater. (2024).
[71] Q. Li, A.C. Grover, E.J. Donald, A. Carr, J. Yu, J. Whitfield, M. Nelson, N. Takeshita, A.E. Chang, Simultaneous targeting of CD3 on T cells and CD40 on B or dendritic cells augments the antitumor reactivity of tumor-primed lymph node cells, J. Immunol. 175 (3) (2005) 1424–1432.
[72] Y. Yang, Y. Zhu, K. Wang, Y. Miao, Y. Zhang, J. Gao, H. Qin, Y. Zhang, Activation of autophagy by in situ Zn(2+) chelation reaction for enhanced tumor chemoimmunotherapy, Bioact. Mater. 29 (2023) 116–131.
[73] H. Cui, X. Zhang, Z. Zhang, M. Zhang, T. Zhang, L. Wu, Z. Lu, J. Gao, W. Zhang, Killing three birds with one stone: tumor-membrane-decorated Prussian blue nanovaccines for synergistic management of skin tumors, radiation dermatitis and wounds, Compos. B Eng. (2023) 264.